Dalton Transactions

COMMUNICATION

View Article Online
View Journal | View Issue

Cite this: *Dalton Trans.*, 2015, **44**, 2997

Received 14th December 2014,
Accepted 6th January 2015

DOI: 10.1039/c4dt03835e

www.rsc.org/dalton

Mesoporous Mn–Zr composite oxides with a crystalline wall: synthesis, characterization and application†

Zhichao Miao,[a,b] Huahua Zhao,[a] Jian Yang,[a] Jun Zhao,[a] Huanling Song[a,c] and Lingjun Chou*[a,c]

Mesoporous Mn–Zr composite oxides (M–MnZr) with a crystalline wall were designed and achieved by a facile one-pot evaporation-induced self-assembly (EISA) strategy. As proved by XRD, HRTEM and SAED characterization, the wall of the obtained mesoporous materials exhibited a typical tetragonal phase of ZrO_2. In addition, the introduced manganese species were homogeneously dispersed in the mesoporous skeleton. N_2-physisorption and TEM results showed that all the final materials possessed an obvious mesoporous structure accompanied by a large specific surface area (~120 m^2 g^{-1}), big pore volume (~0.2 cm^3 g^{-1}) and uniform pore size (~4.9 nm). In addition, the liquid phase oxidation was chosen as the test reaction and the excellent catalytic performance of M–MnZr demonstrated their potential applications in oxidation reactions.

1. Introduction

Since the discovery of the M41S family in 1992, mesoporous materials have been widely investigated, owing to their superior textural properties, such as high surface areas, regular pore frameworks with a large pore size and volume.[1–4] On account of the excellent sorption, catalytic, magnetic, electrochemical, optical and biosensing properties of manganese species, its mesoporous materials attract continuous attention in these fields.[5–8] However, most reports about mesoporous manganese based materials are based on the mesoporous siliceous materials, such as MCM-41, SBA-15 and KIT-6.[9,10] The non-siliceous mesoporous manganese based materials with a crystalline wall have potential to be investigated.

Herein, we employed a facile one-pot EISA strategy to synthesize mesoporous Mn–Zr composite oxides (M–MnZr) with different contents of manganese (0–15%). After removing the SDAs at 550 °C, the M–MnZr materials were obtained. The XRD, HRTEM and SAED characterization techniques were employed to investigate the crystalline framework of the pore wall and the dispersion of manganese species. N_2-physisorption and TEM characterization methods were used to clarify the mesoporous properties of materials. In addition, the resulting materials were tested as catalysts in liquid phase oxidation of ethylbenzene. More details would be described specifically in the main text.

2. Experimental section

$(EO)_{106}(PO)_{70}(EO)_{106}$ triblock copolymer (Pluronic F127, M_{av} = 12 600, Sigma-Aldrich), zirconyl chloride octahydrate ($ZrOCl_2{\cdot}8H_2O$, ≥99.5%, Tianjin Fengyue Reagent Company), manganese chloride tetrahydrate ($MnCl_2{\cdot}4H_2O$, ≥99.0%, Sinopharm Chemical Reagent Co. Ltd), ethanol (C_2H_5OH, ≥99.7%, Sinopharm Chemical Reagent Co. Ltd). All the reagents are of A.R. grade and used as received without further purification.

M–MnZr was synthesized *via* a one-pot evaporation-induced self-assembly (EISA) strategy.[11] In a typical procedure of synthesizing M–MnZr, 1.2 g of F127 was employed as structure-directing agents (SDAs) and dissolved in 15 mL of anhydrous ethanol. As the SDAs were completely dissolved, *a* mmol of $ZrOCl_2{\cdot}8H_2O$ and *b* mmol of $MnCl_2{\cdot}4H_2O$ ($a + b = 5$ mmol) were added into the above solution and stirred for 6 h at least. Finally, the solution mixture was transferred to a petri dish (d = 9 cm) to undergo the slow EISA process at 60 °C for 48 h, then at 100 °C for 24 h in a drying oven. The obtained xerogel was calcined at 550 °C for 6 h to remove the SDAs. The obtained template-free self-assembled M–MnZr was denoted as M–XMnZr and the nominal molar ratio X% = $(b/(a + b) \times 100\%)$.

[a]*State Key Laboratory for Oxo Synthesis and Selective Oxidation, Lanzhou Institute of Chemical Physics, Chinese Academy of Sciences, Lanzhou 730000, People's Republic of China. E-mail: ljchou@licp.cas.cn; Fax: +86 0931 4968129; Tel: +86 0931 4968066*

[b]*University of Chinese Academy of Sciences, Beijing 100049, People's Republic of China*

[c]*Suzhou Institute of Nano-Tech and Nano-Bionics, Chinese Academy of Sciences, Suzhou 215123, People's Republic of China*

†Electronic supplementary information (ESI) available: The reaction formula of liquid phase oxidation of ethylbenzene; N_2-physisorption and TEM characterization of the used catalyst. See DOI: 10.1039/c4dt03835e

Thermogravimetric-differential scanning calorimetry (TG-DSC) measurements were carried out on a NETZSCH STA 449F3 thermogravimetric analyzer from room temperature to 1000 °C with the rate of 10 °C min^{-1} under an air atmosphere. Powder X-ray diffraction (XRD) measurements were performed using an X'Pert Pro Multipurpose diffractometer (PANalytical, Inc.) with Cu Kα radiation (0.15406 nm) at room temperature from 10.0° to 80.0°. The nitrogen adsorption and desorption isotherms at −196 °C were recorded on an Autosorb-iQ analyzer (Quantachrome Instruments U.S.). The specific surface areas were calculated *via* the Brunauer–Emmett–Teller (BET) method in the relative pressure range of 0.05–0.3. The single-point pore volume was calculated from the adsorption isotherm at a relative pressure of 0.990. Pore size distributions were calculated using adsorption branches of nitrogen adsorption–desorption isotherms by the Barrett–Joyner–Halenda (BJH) method. Transmission electron microscopy (TEM), high-resolution transmission electron microscopy (HRTEM), selected area electron diffraction (SAED) and energy-dispersive X-ray spectroscopy (EDX) measurements were performed on a TECNAI G^2 F20 high-resolution transmission electron microscope under a working voltage of 200 kV. The element compositions were analyzed by X-ray Fluorescence (XRF) spectrometry on a Magix PW2403 (PANalytical, Inc.).

The liquid phase oxidation of ethylbenzene was carried out in a round bottom flask fitted with a water condenser. Initially, M–XMnZr (200 mg), acetonitrile (15 mL), ethylbenzene (9 mmol) and *tert*-butyl hydroperoxide (36 mmol) were added into a 50 mL round bottom flask. Then the reaction mixture was stirred at 80 °C for 12 h and the products were centrifuged and extracted with ether. The conversion of ethylbenzene and the selectivity of products were monitored using a gas chromatography (GC) instrument (Agilent-7890A; equipped with a flame ionization detector (FID) and HP-5 column (30 m × 0.32 mm × 0.25 μm)) using octane as the external reference. A gas chromatography-mass spectroscopy (GC-MS) instrument (5975c vl MSD with a triple-axis detector, GC Agilent-7890A) was employed to identify the reaction products. The separated catalyst was washed with ether and activated at 400 °C for 3 h for regeneration.

3. Results and discussion

TG-DSC profiles of the as-synthesized M–MnZr sample recorded in air were first employed to investigate the calcination process. As shown in Fig. 1, the TG curve of the as-synthesized M–10MnZr had three stages for the weight loss and the DSC curve had one endothermal peak and three exothermic peaks at different temperatures. The first weight loss step (~3 wt%) accompanied by an endothermal peak at 50–200 °C was observed. This was attributed to the loss of physically adsorbed water and other volatile species generated in the EISA process. The second step represented the largest weight loss (~55 wt%) and two obvious exothermic peaks in the range 200–350 °C. This was caused by the decomposition of SDAs

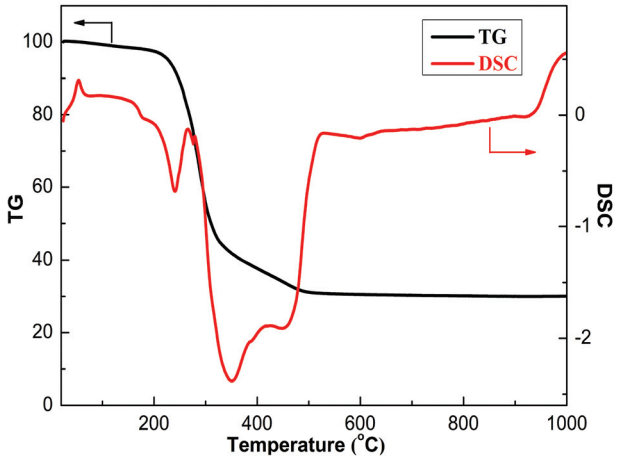

Fig. 1 TG-DSC profiles of the as-synthesized M–10MnZr.

(F127). The last weight loss step (~10 wt%) and an exothermic peak at 350–510 °C might be related to the dehydroxylation of –OH during the formation of the crystalline structure. After 510 °C, there was no obvious weight loss in the TG profile, implying the SDAs were completely removed.

The crystalline structure of M–MnZr after removing the SDAs was investigated by the XRD technology. As shown in Fig. 2, obvious diffraction peaks could be clearly observed in these XRD patterns, indicating the nanocrystalline nature of the obtained M–MnZr. For the M–2MnZr sample, there existed two groups of diffraction peaks. The strong diffraction peaks at 30.2°, 35.0°, 50.3°, 60.2° and 74.8° (JCPDS card no. 80-0784) belonged to the ZrO_2 with the tetragonal phase (t-ZrO_2). The weak diffraction peaks which belonged to the ZrO_2 with the monoclinic phase (m-ZrO_2) appeared at 24.1°, 28.3°, 40.9° and 55.5° (JCPDS card no. 83-0944). This indicated that the pore wall mainly existed as the type of t-ZrO_2 and still existed as a part of m-ZrO_2 in the M–2MnZr sample. Further increasing the

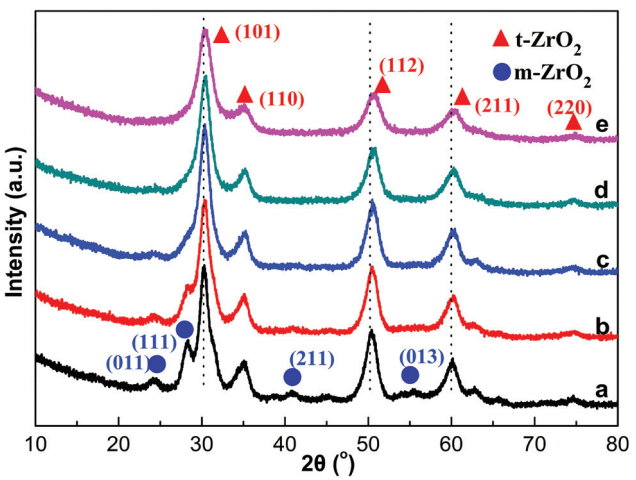

Fig. 2 XRD patterns of M–XMnZr: (a) M–2MnZr, (b) M–5MnZr, (c) M–7MnZr, (d) M–10MnZr, (e) M–15MnZr.

Table 1 Textural properties of M–MnZr obtained from N_2-physisorption, XRD and catalytic performance in liquid phase oxidation of ethylbenzene

	N_2-physisorption			XRD		Catalytic performance	
Samples	Specific surface area ($m^2\ g^{-1}$)	Pore size (nm)	Pore volume ($cm^3\ g^{-1}$)	Interplanar spacing of (101) (nm)	Average crystalline sizes (nm)	Conversion of EB (%)	Selectivity of AP (%)
M–2MnZr	113.0	4.89	0.18	0.297	6.10	52.6	44.1
M–5MnZr	120.1	4.90	0.19	0.296	5.45	67.6	67.1
M–7MnZr	115.6	4.89	0.18	0.295	5.37	80.0	80.1
M–10MnZr	119.0	4.89	0.17	0.295	5.08	82.2	88.8
M–15MnZr	130.3	4.90	0.18	0.294	4.46	80.0	84.0

manganese contents to 5, 7, 10 and 15%, the peaks of m-ZrO_2 became inconspicuous and completely vanished in the M–10MnZr sample. This might be owing to that the introduced manganese species were in favor of maintaining the crystalline phase and preventing the transformation of the pore wall from t-ZrO_2 to m-ZrO_2. In addition, the diffraction peaks of t-ZrO_2 became broader and the average crystalline sizes calculated from the Scherrer equation (shown in Table 1) became smaller with the increasing manganese contents. Moreover, the position of diffraction peaks slightly shifted to higher 2θ values with the introduction of manganese species. This phenomenon implied that the interplanar spacing and cell parameters became smaller because of the isomorphous of zirconium with manganese species, which had a smaller ionic radius (0.53, 0.64, 0.83 Å for Mn^{4+}, Mn^{3+}, Mn^{2+} and 0.84 Å for Zr^{4+}).[12,13] In addition, it is noteworthy that there were no diffraction peaks related to the manganese species in the XRD patterns. This might be owing to that the introduced manganese species were highly dispersed in the mesoporous skeleton of M–MnZr. The highly dispersed manganese species might offer plentiful active sites for the reactants.

The mesoporous structure and textural properties of M–MnZr with different manganese contents were characterized by N_2-physisorption. N_2 adsorption–desorption isotherms and pore size distributions (PSD) are shown in Fig. 3. It was observed that all the samples displayed the typical IV isotherm curve, which was the characteristic of mesoporous materials. Meanwhile, the hysteresis loops of all the samples were intermediate between typical H1 and H2-type in the P/P_0 range from 0.4 to 0.8, suggesting the presence of cage-like mesopores or mesopores with constriction. In addition, all the isotherms exhibited steep capillary condensation steps, which indicated the presence of uniform mesopores. This also could be further confirmed from the PSD and TEM images. As shown in Fig. 3(2), the pore size narrowly distributed around 5 nm, once again reflecting the presence of uniform mesopores and the pore dimension is in good agreement with the following TEM images. Moreover, the textural properties of M–MnZr obtained from N_2 adsorption–desorption isotherms are given in Table 1. All the samples showed excellent textural properties with a large specific surface area (~120 $m^2\ g^{-1}$), uniform pore size (~4.9 nm) and a large pore volume (~0.2 $cm^3\ g^{-1}$). In addition,

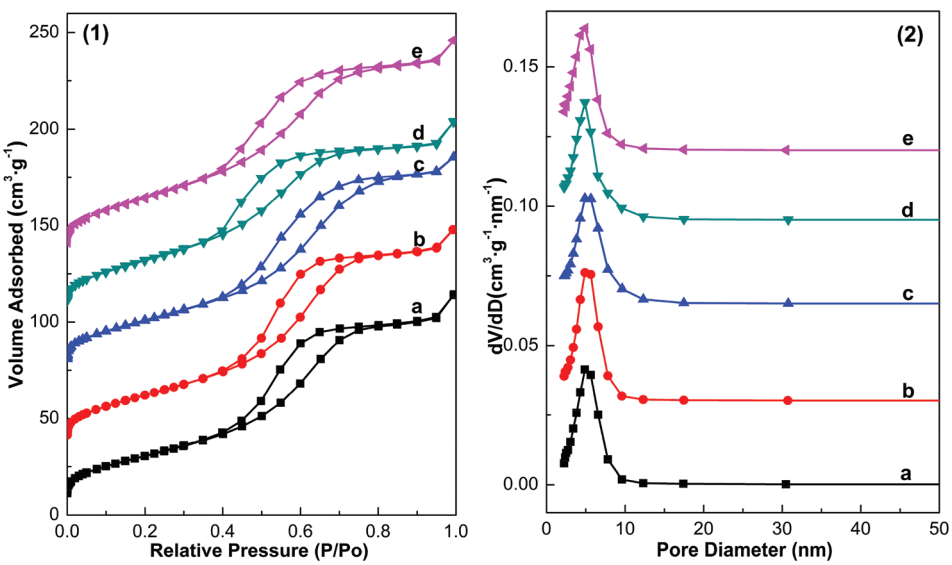

Fig. 3 (1) N_2-physisorption isotherms and (2) pore size distributions of M–XMnZr: (a) M–2MnZr, (b) M–5MnZr, (c) M–7MnZr, (d) M–10MnZr, (e) M–15MnZr.

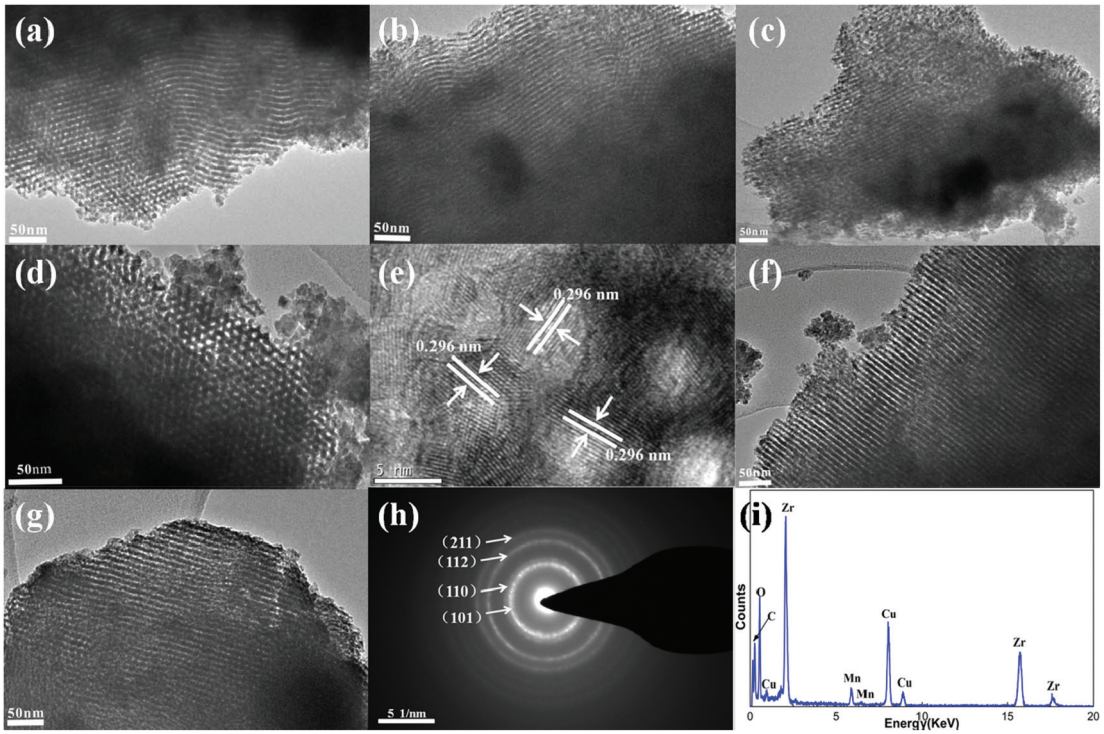

Fig. 4 TEM images of M–XMnZr: (a) M–2MnZr, (b) M–5MnZr, (c) M–7MnZr, (d, f) M–10MnZr, (g) M–15MnZr; (e) HRTEM image; (h) SAED pattern and (i) EDX measurement of M–10MnZr.

the textural parameters changed little with the increasing manganese contents. This might be due to that the manganese species were highly dispersed in the mesoporous walls and had little influence on the mesoporous structure.

TEM images were obtained to further confirm the presence of mesopores in M–MnZr. As shown in Fig. 4, all the samples with different manganese contents showed an obvious mesoporous structure along [110] and [001] orientations. This phenomenon further confirmed the prediction of N_2-physisorption. In addition, as shown in Fig. 4e, a highly crystalline mesoporous framework could be clearly observed and the lattice spacing obtained from the HRTEM image was 0.296 nm, keeping consistent with the value of 0.295 nm for the (101) planes of t-ZrO_2 in the XRD patterns. As shown in Fig. 4h, the SAED analysis of M–10MnZr, which exhibited obvious diffraction rings, further confirmed that the pore walls of the obtained materials were made up of nanocrystalline oxides. In addition, the *d*-spacing values obtained from SAED diffraction rings are in good agreement with the (101), (110), (112) and (211) planes of t-ZrO_2 in the XRD patterns. In the EDX measurement of M–MnZr (Fig. 4i), the exclusive peaks of Mn and Zr elements were obviously observed in the pattern, showing that all the elements were successfully introduced into the framework of the mesostructure.

The M–MnZr materials were employed as catalysts for the liquid phase oxidation of ethylbenzene (as shown in Fig. S1†), which was an important reaction in pharmaceutical and fine-chemical industries.[14,15] As shown in Table 1, the conversion of ethylbenzene (EB) and the selectivity of acetophenone (AP) were gradually improved with the increasing manganese contents and the optimal catalytic performance was obtained at 10% manganese content with 82.2% conversion of EB and 88.8% selectivity of AP. The excellent catalytic performance might be owing to the highly dispersed manganese species, which could offer sufficient active sites for the reactants.

As for a promising heterogeneous catalyst, the heterogeneity and recyclability of M–10MnZr were investigated. As shown in Fig. 5(1), there was no obvious increase in the yield of AP after removing the catalyst from the reaction system at 4 h. However, the reaction recovered and the yield of AP increased when the catalyst was added again. This indicated that the M–MnZr was truly a heterogeneous catalyst and the reaction was only being possible in the presence of M–MnZr. Meanwhile, compared with the fresh catalyst (10.6%), the Mn contents showed little change in the used catalyst (10.8%), demonstrating that no obvious manganese species leached into the liquid phase in the reaction process.

The M–10MnZr was recycled for five runs to evaluate the recyclability of the catalyst and the results are shown in Fig. 5(2). Compared with the fresh catalyst, no significant decrease occurred in the catalytic performance even after five runs, showing that the M–MnZr could be reused as a heterogeneous catalyst in the liquid phase oxidation of EB. In addition, the regenerated catalyst was characterized by N_2-physisorption and TEM (shown in Fig. S2 and S3†). The results manifested that the mesoporous structure with excellent textural properties (specific surface area (99.9 $m^2\ g^{-1}$), pore size (4.90 nm) and volume (0.15 $cm^3\ g^{-1}$)) and the crystalline pore

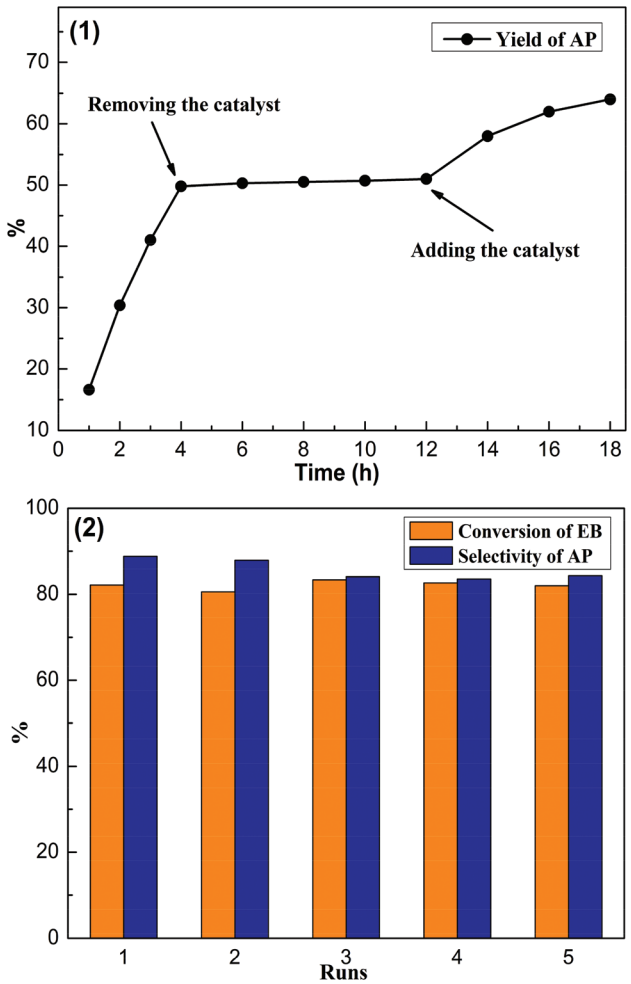

Fig. 5 Liquid phase oxidation of ethylbenzene: (1) heterogeneity and (2) recyclability of M–10MnZr.

wall structure was successfully maintained. The catalyst showed excellent stability in the reaction process. These results implied that M–MnZr could be employed as a catalyst for selective oxidation reaction.

4. Conclusion

In this paper, a facile and general one-pot EISA strategy was employed to synthesize a series of M–MnZr with different manganese contents. The obtained materials had excellent mesoporous structures, crystalline walls and highly dispersed manganese species. In addition, the M–MnZr showed excellent catalytic performance in the liquid phase oxidation of ethylbenzene.

Acknowledgements

The authors sincerely acknowledge the financial support from the "Strategic Priority Research Program" of the Chinese Academy of Sciences, Grant no. XDA09030101 and the National Natural Science Foundation of China (no. 21133011, 21373244).

Notes and references

1 C. T. Kresge, M. E. Leonowicz, W. J. Roth, J. C. Vartuli and J. S. Beck, *Nature*, 1992, **359**, 710–712.
2 D. Gu and F. Schüth, *Chem. Soc. Rev.*, 2014, **43**, 313–344.
3 J. Tang, N. L. Torad, R. R. Salunkhe, J. H. Yoon, M. S. Al Hossain, S. X. Dou, J. H. Kim, T. Kimura and Y. Yamauchi, *Chem. – Asian J.*, 2014, **9**, 3238–3244.
4 J. Tang, J. Liu, C. Li, Y. Li, M. O. Tade, S. Dai and Y. Yamauchi, *Angew. Chem., Int. Ed.*, 2015, **54**, 588–593.
5 N. Pal, E. B. Cho, D. Kim and M. Jaroniec, *J. Phys. Chem. C*, 2014, **118**, 15892–15901.
6 G. Giribabu, G. Murali and R. P. Vijayalakshmi, *Mater. Lett.*, 2014, **117**, 298–301.
7 F. J. Brieler, P. Grundmann, M. Fröba, L. Chen, P. J. Klar, W. Heimbrodt, H. A. Krug von Nidda, T. Kurz and A. Loidl, *Chem. Mater.*, 2005, **17**, 795–803.
8 Y. Chen, H. Chen, S. Zhang, F. Chen, S. Sun, Q. He, M. Ma, X. Wang, H. Wu, L. Zhang, L. Zhang and J. Shi, *Biomaterials*, 2012, **33**, 2388–2398.
9 Q. Zhang, Y. Wang, S. Itsuki, T. Shishido and K. Takehira, *J. Mol. Catal. A: Chem.*, 2002, **188**, 189–200.
10 H. Pérez, P. Navarro, J. J. Delgado and M. Montes, *Appl. Catal., A*, 2011, **400**, 238–248.
11 Q. Yuan, L. L. Li, S. L. Lu, H. H. Duan, Z. X. Li, Y. X. Zhu and C. H. Yan, *J. Phys. Chem. C*, 2009, **113**, 4117–4124.
12 S. Azalim, M. Franco, R. Brahmi, J. M. Giraudon and J. F. Lamonier, *J. Hazard. Mater.*, 2011, **188**, 422–427.
13 J. Zuo, Z. Chen, F. Wang, Y. Yu, L. Wang and X. Li, *Ind. Eng. Chem. Res.*, 2014, **53**, 2647–2655.
14 S. Velusamy, M. Ahamed and T. Punniyamurthy, *Org. Lett.*, 2004, **6**, 4821–4824.
15 P. Visuvamithiran, K. Shanthi, M. Palanichamy and V. Murugesan, *Catal. Sci. Technol.*, 2013, **3**, 2340–2348.